PHYSICS

Undepleted direct laser acceleration

Itamar Cohen[1,2], Talia Meir[1,2,3], Kavin Tangtartharakul[4], Lior Perelmutter[1,2], Michal Elkind[1,2], Yonatan Gershuni[1,2], Assaf Levanon[1,2], Alexey V. Arefiev[4], Ishay Pomerantz[1,2]*

Intense lasers enable generating high-energy particle beams in university-scale laboratories. With the direct laser acceleration (DLA) method, the leading part of the laser pulse ionizes the target material and forms a positively charged ion plasma channel into which electrons are injected and accelerated. The high energy conversion efficiency of DLA makes it ideal for generating large numbers of photonuclear reactions. In this work, we reveal that, for efficient DLA to prevail, a target material of sufficiently high atomic number is required to maintain the injection of ionization electrons at the peak intensity of the pulse when the DLA channel is already formed. We demonstrate experimentally and numerically that, when the atomic number is too low, the target is depleted of its ionization electrons prematurely. Applying this understanding to multi-petawatt laser experiments is expected to result in increased neutron yields, a perquisite for a wide range of research and applications.

INTRODUCTION

Laser wakefield acceleration (LWFA) has brought giga–electron volt particle beams to university-scale laboratories. In LWFA, plasma waves excited by an ultrashort laser pulse propagating through an under-dense plasma trap and accelerate electrons to relativistic velocities. For the past two decades, the LWFA community focused on optimizing the accelerated beam quality for higher particle energy (*1*–*3*), sharper energy spectrum (*4*, *5*), higher charge (*6*, *7*), and improved repeatability (*8*). Applications for LWFA electron beams (*9*) are now becoming a reality (*10*).

In contrast to LWFA, direct laser acceleration (DLA) relies on the electrons gaining energy from the laser fields themselves. In DLA, the electron beam is formed in a positively charged plasma channel that was partially vacated of electrons by the ponderomotive pressure exerted by the laser pulse (*11*). Strong quasi-static azimuthal magnetic fields are generated through the driving of longitudinal electron currents by the intense laser pulse. These quasi-static fields mitigate the longitudinal dephasing between the electrons and the laser beam that would have otherwise taken place in vacuum (*12*), enabling the electrons to gain energy. The lack of correlation between the acceleration of electrons and plasma wave production has been established by measurements of the transmitted laser spectrum (*13*). Oscillations of these electrons in the channel consequently also generate synchrotron x-rays (*14*) and transition radiation in the terahertz range (*15*).

DLA of electrons has been observed experimentally for over a quarter of a century (*15*–*23*). The energy spectrum of the electron beam follows a Boltzmann-like distribution with an effective temperature in the mega–electron volt range, which scales as the square root of the laser intensity (*24*). Although the continuous spectrum makes DLA less appealing than LWFA for certain applications, it features the advantage of extremely high conversion efficiency (CE) of the incident laser energy to relativistic electrons as high as 23% (*25*).

In DLA, the electron beam temperature is found to peak when the density of the plasma plume is nearing its critical value. Such nearly critical density plasma plumes may be formed by using gas jet systems, which are simple to operate with up to kilohertz rates (*23*), but their material selection is limited, or by using low-density polymer foam targets (*21*, *26*, *27*). Alternatively, plasma plumes with an arbitrary fraction of solid density may be formed by pre-exploding a solid foil, using a second laser "pre-pulse," allowing an expansion time on the order of nanoseconds before irradiation with the main pulse. With shorter delays, this technique is also used to increase laser energy absorption by pre-expanding targets in laser ion acceleration schemes (*28*).

The limited contrast of previous generation lasers hindered the investigation of DLA because precursor light native to the laser system preheated the target in an uncontrolled manner. Modern high-power laser technology now makes possible parametric investigation of DLA from pre-exploded foils (*15*, *21*).

To date, DLA experiments have been performed using low–atomic number ("low-Z") plasma targets only. In this work, we generated electron beams from high-Z plasma plumes created by pre-exploding thin foils of Au and measured substantially higher electron temperatures than those obtained with low-Z targets. As will be presented below, our results reveal that, for efficient DLA to prevail, a target material of sufficiently high atomic number is required to maintain the injection of ionization electrons at the peak intensity of the pulse when the DLA channel is already formed.

RESULTS

In our experiments, we tailored the plasma plume density profile by setting the pre-pulse energy and the pre-pulse to main-pulse delay interval to optimize the generated electron beam charge and energy, as described below. Figure 1A presents measured electron spectra generated from Au (solid curves) and CH (dashed curves) plasmas irradiated with normalized laser pulse intensity in the range of $a_0 =$ 2.6 to 4.4, where $a_0 = |e|E_0/(c\omega m_e)$ is the normalized amplitude of a laser pulse with electric field E_0 and frequency ω.

The extracted electron temperature for both types of plasma is plotted in Fig. 1B versus a_0. Each data point represents an average over one to three shots. The bars signify 11% of systematic uncertainty, which was evaluated from the spread of results taken under the same experimental conditions. For $a_0 > 3.0$, the electron temperature of Au plasma maintains the scaling predicted by Pukhov *et al.* (*11*), while that of CH falls short.

[1]School of Physics and Astronomy, Tel Aviv University, Tel Aviv 69978, Israel. [2]Center for Light-Matter Interaction, Tel Aviv University, Tel Aviv 69978, Israel. [3]School of Electrical Engineering, Tel Aviv University, Tel Aviv 69978, Israel. [4]Department of Mechanical and Aerospace Engineering, University of California, San Diego, La Jolla, CA 92093, USA.
*Corresponding author. Email: ipom@tauex.tau.ac.il

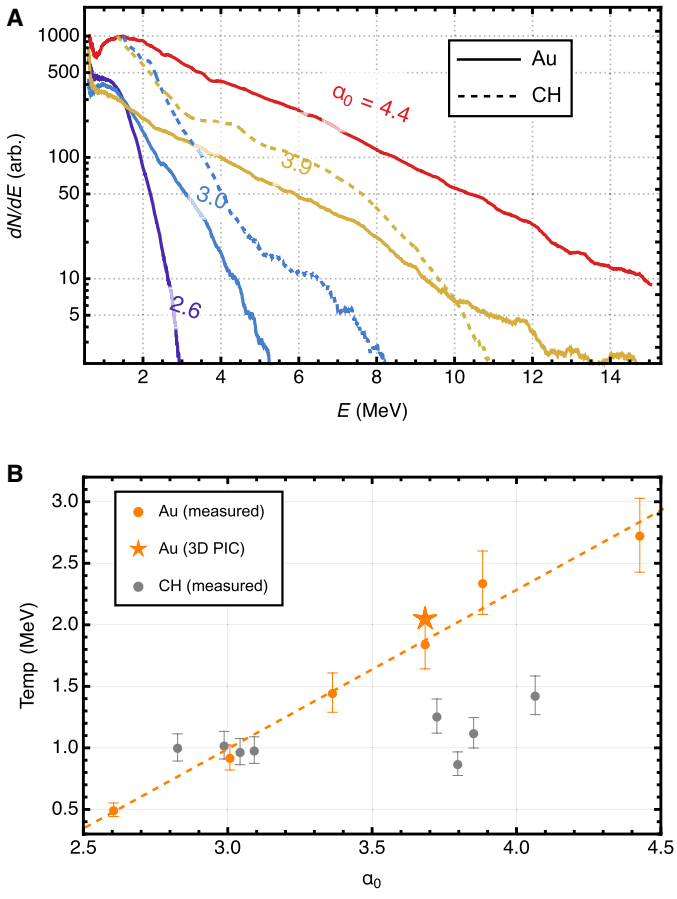

Fig. 1. The energy of DLA electron beams generated from low-*Z* versus high-*Z* targets. (**A**) Measured electron spectra from the irradiation of Au (solid) and CH (dashed) plasma plumes. The respective normalized laser intensities are indicated on the curves. The plumes were formed by pre-exploding 800-nm-thick foils using a pre-pulse at optimal energy and relative delay conditions, as described in the text. (**B**) Fitted electron temperatures as a function of a_0 for the same conditions as in (A). The dashed orange curve shows the linear fit to the Au data, which is in agreement with Pukhov scaling (*11*). The electron temperature obtained from 3D PIC simulation for $a_0 = 3.7$ is also shown (star symbol).

To determine how high–atomic number plasmas maintain the observed acceleration efficiency, we examined the dependence of the electron beam temperature and flux on the density profile of the plume at a fixed intensity. The irradiation setup, shown in cartoon schematics in Fig. 2A and described in detail in Materials and Methods, consists of a double-pulse irradiation scheme. The plasma plume was formed by irradiating a thin foil with a 43-ps-long laser pulse in an energy range of microjoules to millijoules. After allowing the plume to expand for an interval of $\Delta t^{pre}_{main} = 4$ to 90 ns, the plasma was irradiated by a 30-fs-long laser pulse of normalized intensity in the range of $a_0 = 2.6 - 4.4$. Under these different irradiation conditions, we recorded interference images of the density profile of the plume, the near-field image of light punching through the plume, and the emitted electron beam energy spectrum using a magnetic spectrometer (see Materials and Methods).

Figure 2B presents these measured properties for plumes generated by a 1.9-mJ pre-pulse, $a_0 = 2.9$ main pulse, and different Δt^{pre}_{main} delays. The electron flux (for electrons above an energy threshold of 0.5 MeV) is plotted versus the plume's peak density, in units of the critical density. The falloff of the electron spectrum was fitted to a Maxwellian distribution (discussed further below), whose temperature is indicated by the data point's color. A near-field image of light punching through the plasma is shown above each data point. As expected, the plasma becomes more transparent to the laser light as its density falls below the critical value. The main observation is that there exists a Δt^{pre}_{main} value, at which both the electron beam temperature and flux peak. The data presented in Fig. 1 were obtained using the pre-pulse condition that yielded the highest electron temperature.

Upon irradiation by an intense laser pulse, a thin solid foil turns into an expanding plume of plasma. Such plumes have been studied both numerically (*29*) and in experiments (*30*, *31*). To predict the plume's density profile for arbitrary Δt^{pre}_{main} and *Epp* values, the measured plasma density profiles were fitted to the form

$$n_i = n_{i0}\frac{R_0^2}{R^2(t)}\frac{L_0}{L(t)}\left[1+\sqrt{\alpha}|z|/L(t)\right]^{1/\alpha} e^{-\frac{r^2}{R(t)^2}} e^{-\frac{|z|}{\sqrt{\alpha}L(t)}} \quad (1)$$

Here, n_{i0} is the initial solid density; R_0 is the initial radius of the plume; $L_0 = c_s\tau_{pp}$ is the initial plasma longitudinal scale length; c_s is the ion acoustic velocity; $R(t)$ and $L(t)$ are its radial and longitudinal scale lengths, respectively; and z and r are coordinates of a cylindrical system aligned with the laser propagation direction. The requirement of ion number conservation with the initial target foil of thickness d, $\int n_i dV = n_{i0}R_0^2 d\pi$, sets the value of the shape factor α, $N_\alpha = \sqrt{\alpha}\sqrt[\alpha]{\alpha\cdot e}\Gamma(1+1/\alpha, 1/\alpha) = \frac{d}{2L_0}$, where Γ is the incomplete gamma function.

We parameterize the scale-length dependence on the pre-pulse energy and expansion time as

$$\begin{cases} R(E_{pp},t) = A_R\left(\frac{E_{pp}}{1\,\mu J}\right)^{B_r} \\ \sqrt{\alpha(E_{pp})}L(E_{pp},t) = A_L\left(\frac{E_{pp}}{1\,\mu J}\right)^{B_L}\left(\frac{t}{1\,ns}\right) \\ n_i(E_{pp},t) = A_n q\left(\frac{E_{pp}}{1\,\mu J}\right)^{B_n}\left(\frac{t}{1\,ns}\right)^{-1} \end{cases} \quad (2)$$

The fitted values of the parameters A_R, B_R, A_L, B_L, A_n, and B_n are given in Table 1. Their uncertainty values signify one SD of the fitting procedure.

We note that, in the scope of this paper, Eqs. 1 and 2 are given as a parameterization of the measured density profiles. However, Eq. 1 is an approximate solution to the plasma equations of motion in the limit of $\alpha \ll 1$, which evolves with time according to Eq. 2. This will be the subject of a future publication.

To reveal the underlying laser plasma dynamics, we used particle-in-cell (PIC) simulations carried out with the EPOCH code (see Materials and Methods for details) (*32*). The density profile before the interaction with the main pulse (Eq. 1) served as the initial state in these simulations. The targets were representative of electrons and singly ionized Au ions with $R = 93.6$ μm and $\alpha = 0.11$. The values for L and n_0 used to generate the simulation results presented here are tabulated in Table 2.

One such density profile, which, in the simulations, yielded the highest electron temperature under irradiation by an $a_0 = 3.7$ laser

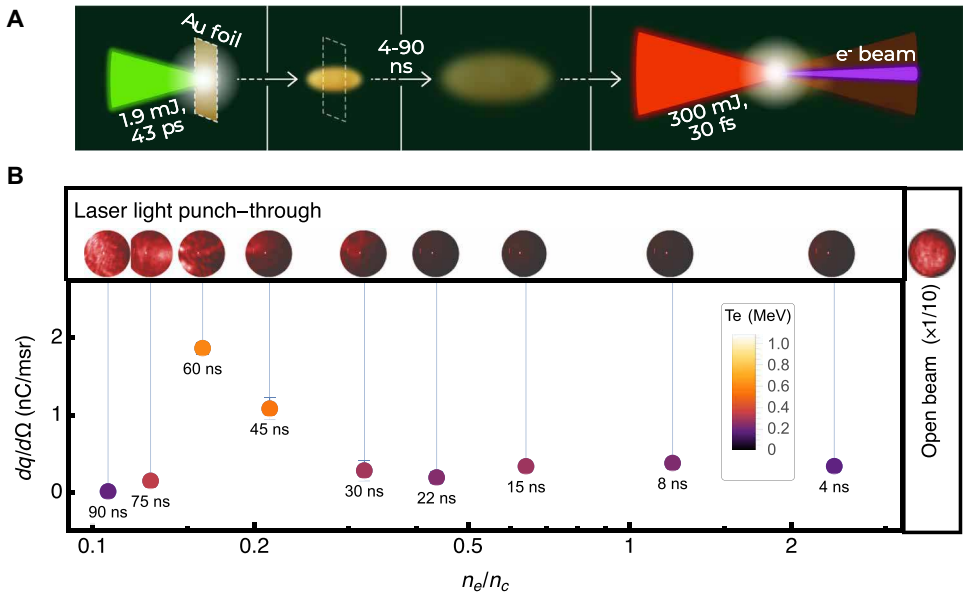

Fig. 2. Electron beam dependence on the target expansion time. (**A**) Cartoon schematic of the irradiation setup. A plasma plume is formed out of a thin Au foil that is irradiated by a 43-ps-long laser pulse with 1.9 mJ of energy. The density of the plume is controlled by the interval (Δt^{pre}_{main} = 4 to 90 ns) over which the plume expands into vacuum before interacting with the $a_0 = 2.9$ intensity main laser pulse. (**B**) The measured charge per unit solid angle at the laser incident direction, as a function of the peak density of the plume. The color scale indicates the temperature that characterizes the falloff of the high-energy end of the electron beam spectrum. Near-field images of light punching through the plume are shown about each data point.

Table 1. Parameterization values for the density profiles described by Eq. 2.

A_R (μm)	B_R	A_L (μm)	B_L	$A_n(n_c)$	B_n
1.81 ± 0.34	0.523 ± 0.043	(2.57 ± 0.94) · 10^{-3}	0.663 ± 0.064	2.2 ± 5.3	−0.28 ± 0.41

Table 2. Peak electron density and longitudinal scale values used as the initial conditions for the PIC simulations presented in Figs. 3 and 4.

Δt^{pre}_{main}	(ns)	5	10	30	45	60	90
n_{e0}	(10^{19}cm^{-3})	9.01	4.51	1.50	1.00	0.75	0.50
L	(μm)	5.53	11.07	33.21	49.83	66.42	99.64

pulse, is plotted in Fig. 3A. Subsequent field ionization by the main laser pulse was implemented in EPOCH using a Monte Carlo algorithm, in which barrier suppression and tunneling ionization probabilities were obtained from a generalized tunneling model (*33*, *34*). Full details of the implementation are given in (*35*). The computational load of this implementation allowed us to run one simulation in three dimensions (3D), for this irradiation condition, which resulted in the data point marked with a star symbol in Fig. 1B. A parametric scan for different plume conditions, which is described below, was conducted by running the simulations in 2D. Figure 3B shows three temporal snapshots of the transverse component of the electric field, averaged over four optical cycles of the laser. A positively charged plasma channel starts to form on the first snapshot, as can be seen by the outward-pointing quasistatic transverse field: positive values (red) for $y > 0$ and negative values (blue) for $y < 0$. For these same snapshots, Fig. 3 (C to F) presents density distributions corresponding to electrons originating from the $Z = 17$, 28, 33, and 39 ionization levels of Au. Such extremely high ionization levels have been observed also in, e.g., nanostructured Au targets (*36*) irradiated with similar laser intensities. Beyond $Z \geq 40$, negligible ionization is observed in the simulations. A spatial distribution of the average electron energy is overlaid in red on each of these plots. It is evident that ionization of low-Z–level electrons commences early and forms clear wake structures (Fig. 3C), but these electrons are ionized before the creation of the channel and, therefore, are not trapped and never reach high energies. Electrons from higher ionization levels (Fig. 3, E and F), which are ionized later, when the electric field is maximal and the channel is already formed, reach high kinetic energies. Repeating these simulations while limiting the target ionization up to the $Z = 15$ ionization level resulted in low electron beam temperatures, thus confirming this observation.

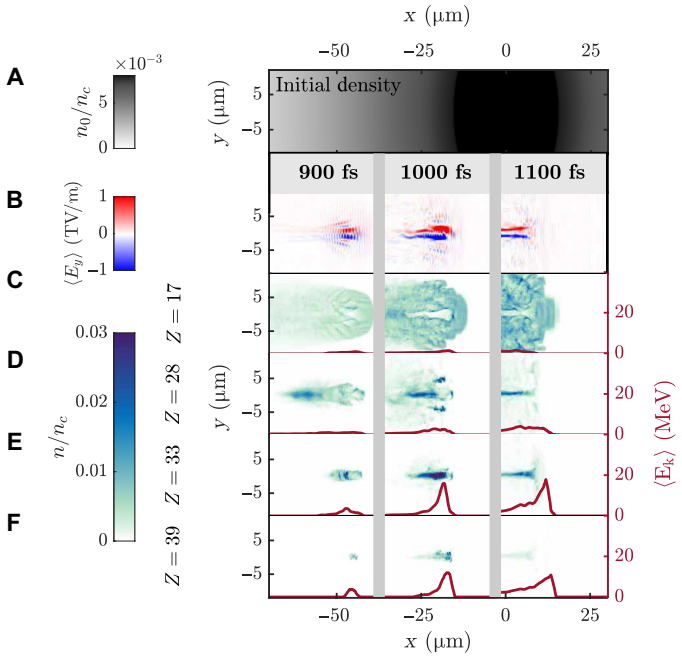

Fig. 3. Results of a PIC simulation. The initial plasma plume profile in this simulation yielded the highest amount of energetic electrons under irradiation by an $a_0 = 3.7$ laser pulse. (**A**) Spatial distribution of the initial electron density plume, obtained from the fit to the measurement taken with $\Delta t^{pre}_{main} = 30$ ns. (**B**) Three temporal snapshots of four-cycle averaged transverse component of the electric field. (**C** to **F**) Density distributions (blue) for electrons ionized from the $Z = 17$, 28, 33, and 39 ionization levels, respectively. Spatially averaged electron energy distributions $\langle E_k \rangle$ are overlaid in red.

The fidelity of the PIC simulations in capturing the experimental observations is enhanced further when inspecting the electron spectra in detail. Figure 4A shows measured electron spectra for the same shots that generated the data points in Fig. 2B.

The spectral content consists of two peaks, which is typical of DLA (*16*). To guide the reader's eye to the evolution of each of the peaks with Δt^{pre}_{main}, the spectra were fitted to a double-Maxwellian form, separately colored in pink and green. Both peaks reach their maximal value when $\Delta t^{pre}_{main} = 45$ to 60 ns, with the high-energy peak being more sensitive to Δt^{pre}_{main}. This evolution may be compared with the results obtained from PIC simulations in Fig. 4B, which presents the spectra of electrons ejected from the plasma plume to a distance of 100 μm, having momentum in the forward direction within a cone half-angle of 0.4 rad, with an energy larger than 0.5 MeV. Here, the two peaks are apparent as well, and their evolution with Δt^{pre}_{main} follows the one observed in the experiment but with higher overall temperatures and a lower Δt^{pre}_{main} at which they peak. The overall higher electron energies that we observe in these 2D simulation, compared to 3D (Fig. 1B) and the experiment, are typical to these studies (*37*).

The dynamics responsible for accelerating high-Z electrons to high energies is identified by first dividing each spectrum in Fig. 4B into two electron populations, labeled "L" for LWFA and "D" for DLA, according to whether most of the integrated work was performed on the electrons is parallel or transverse to the laser direction (*18*, *38*); see further details in Materials and Methods. Within each of these subpopulations, the spectra are color-coded according to the ionization level from which they emerged. We observe that the high-temperature peak, which, in the simulation, rises at $\Delta t^{pre}_{main} =$ 30 ns, consists mostly of high-Z electrons undergoing DLA.

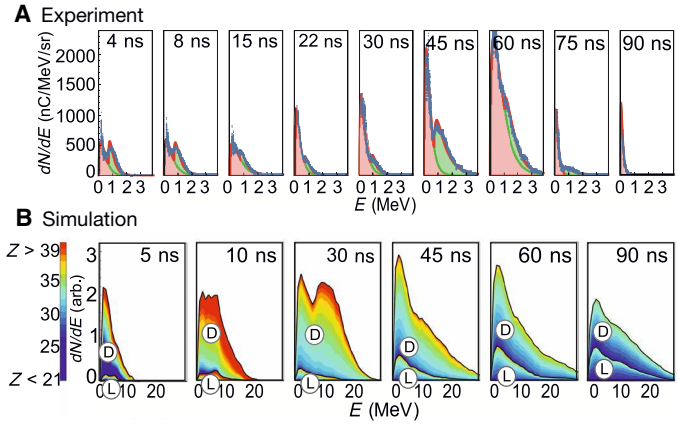

Fig. 4. The generated electron spectra details for rising target expansion times. Measured (**A**) and simulated (**B**) electron spectra for the same irradiation conditions as in Fig. 2. The measured spectra (A) are fitted to a double-Maxwellian form. The Maxwellian components are colored in pink and green to guide the eye on their respective evolution with Δt^{pre}_{main}. The simulated spectra (B) are subdivided into parts dominated by DLA or LWFA indicated by D and L, respectively. Within these subpopulations, the spectra are color-coded according to the ionization level of the plasma from which they originate.

Figure 4B indicates that, for shorter and denser plasma plumes, like for $t^{pre}_{main} = 10$ ns, a large population of electrons from high ionization levels undergo DLA but do not reach the high energies obtained from longer plumes like for $t^{pre}_{main} \geq 30$ ns. To understand the interplay between the ionization level origin and the final electron energies for different plume sizes, we present in Fig. 5 longitudinal

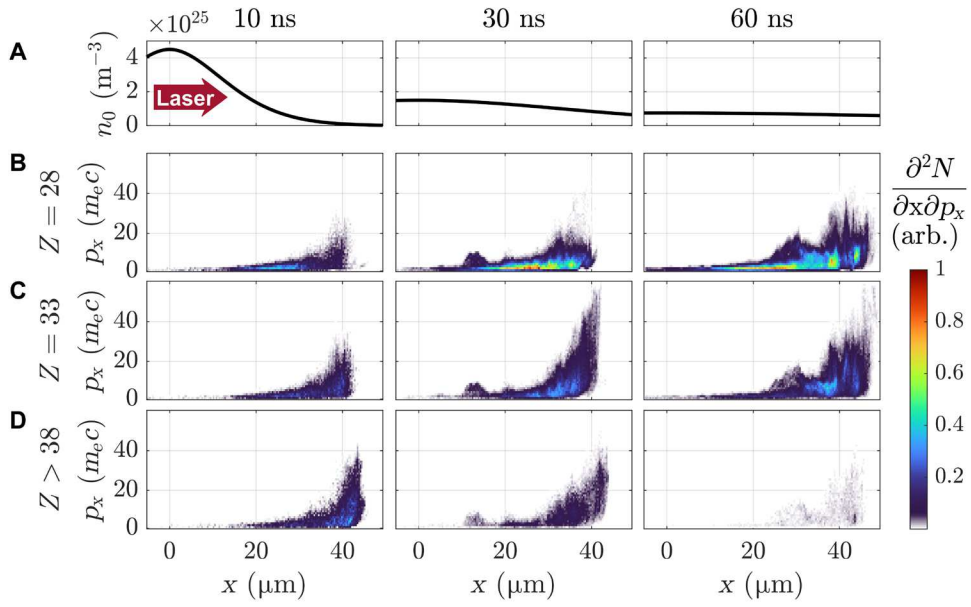

Fig. 5. The interplay between ionization levels and effective DLA. (**A**) The initial plasma density profile for three plasma plumes, created with expansion times of t^{pre}_{main} = 10, 30, and 60 ns. (**B** to **D**) Longitudinal phase space density snapshots at t = 1200 fs, for Z = 28, Z = 33, and Z > 38, respectively.

phase space plots of the electrons at t = 1200 fs, separated into their ionization level origin (Z = 28, Z = 33, and Z > 38). Also shown are the plumes' initial density profiles. For shorter denser plumes, the laser fields undergo stronger self-focusing and ionization of deeper levels occur. However, the DLA channels are shorter, and the acceleration results in lower final energies. For longer plumes of lower density, such as for t^{pre}_{main} = 60 ns, the field amplitudes are able to ionize only lower atomic levels, but acceleration occurs over a longer distance. Maximal energies are observed for the t^{pre}_{main} = 30-ns plume, where electrons originating from the Z = 33 level accelerate over a large distance.

Another feature observed in Fig. 5 is the energy chirp that develops for electrons originating from higher ionization levels, as a consequence of their later ionization time. For the optimal acceleration conditions of t^{pre}_{main} = 30 ns, a negative energy chirp with absolute value smaller than 1 MeV fs^{-1} is observed.

Both LWFA and DLA are known to coexist in nearly critical density plasmas irradiated with high-power lasers, when a substantial overlap between the transverse laser field and the trapped electrons prevails (*39*). This overlap may be quantified by the dimensionless parameter $T_p = \omega_p \tau_{laser} / (2\pi\sqrt{a_0})$, where $T_p \approx 1$ indicates a substantial overlap. For the dataset presented in Figs. 2B and 4A, T_p drops from a value of 6.8 at low pre-pulse delays to 1.75 in optimal conditions at 60 ns.

The CE from laser energy to electrons and the divergence and pointing stability of the electron beam are paramount for the applicability of a DLA electron source as a photonuclear reaction generator. Using a wide angular acceptance spectrometer, which consisted of a 1.2 cm (horizontal)–by–400 μm (vertical)–wide slit with a magnetic-field strength of 0.15 T, positioned 3.5 cm downstream from the target, we determined the electron beam to have an ~10 msr divergence, and to be slowly focusing with rising laser intensities, as also observed by others (*40*).

We measured the pointing stability of the electron beam in our experiments to be 8.2 mrad (root mean square), lower than the beam divergence and notably lower than that reported in (*22*, *26*, *41*). This difference is likely due to the low pre-pulse energy (1.9 mJ) and long Δt^{pre}_{main} interval (60 ns). By contrast, those other experiments used pre-pulse energies of 16 to 3000 mJ, which dictated Δt^{pre}_{main} of only a few nanoseconds.

By calibrating the absolute light emission of the electron spectrometer using a ^{90}Sr calibration beta emitter, we retrieved the CE of laser energy to electrons (above an energy threshold of 0.5 MeV). For Au plasma at the highest laser intensity available to us of a_0 = 4.5, the CE was larger than 10%. This value is not much lower than what we and others have observed in petawatt (PW)-level DLA experiments (*20*, *22*); therefore, we expect that much higher values can be achieved with irradiation of high-Z plasmas under optimized conditions at the PW level.

To demonstrate photoneutron generation, we placed a 1-cm-thick sample of ^{238}U 5.5 cm downstream from the target. Bremsstrahlung radiation, produced by the electron beam stopping in the sample, induced photonuclear reactions in the sample resulting in neutron emission. We measured the neutron flux using five Bubble dosimeters (Bubble technology industries) positioned 26 cm downstream from the ^{238}U converter outside the vacuum vessel. The neutron flux was determined with the same procedure described in (*20*, *42*) and was found to be 7.1 × 10^5 neutrons per Joule of laser energy.

DISCUSSION

In the work presented here, we show that ionization injection in DLA becomes inefficient when the plasma is depleted of new electrons to supply. The practical implication is that to maintain efficient acceleration, targets with sufficiently high atomic number must be matched to the laser intensity. Furthermore, we have shown that using millijoule-level pre-pulses to form the plasma plume and allowing it to expand over a period of tens of nanoseconds results in high pointing stability of the electron beam, notably superior to the shorter expansion times used in other experimental scenarios.

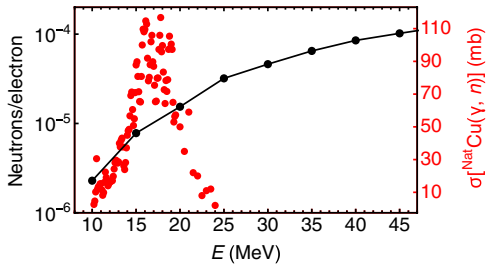

Fig. 6. The efficiency of photoneutron generation using mega–electron volt–level electron beams. Each data point (black) represents the results of a particle transport simulation of a monoenergetic electron beam impinging on a 10-cm-thick Cu block. Shown in red are measured cross sections (*48*) of the ^{Nat}Cu(γ, *n*) reaction.

Past PW-level DLA experiments using low-*Z* plasmas resulted in electron beam temperatures of about 10 MeV (*20*). The photoneutron production cross section in most materials peaks in the range of 10 to 40 MeV (*43*), and so only the high-energy tail of the Bremsstrahlung spectra produced with such electrons induced neutron emission. Our discovery therefore indicates that repeating these experiments with high-*Z* plasmas will increase the photoneutron yields well beyond the temperature scaling in Fig. 1. These increased neutron yields are required to enable a wide range of research and applications, such as investigation of nucleosynthesis in the laboratory (*44*), performing nondestructive material analysis (*45*), and industrial applications (*46*). To illustrate this point, Fig. 6 presents particle transport simulation results of monoenergetic electrons impinging on a 10-cm block of Cu. These simulations were conducted using the FLUKA Monte Carlo package (*47*), with the same methodology described in (*20*). The efficiency of converting electrons to neutrons is plotted in black, and the photoneutron production cross section of Cu (*48*) is shown in red.

On the multi-PW level, the electron energy cutoff in DLA presents a nontrivial dependence on the pulse width and laser focal size (*49*), and radiation reaction of the electrons becomes prominent (*50*, *51*). The *Z*-dependence of DLA discussed here should also be taken into account in, e.g., proposed schemes direct acceleration of positron beams from plasma (*52*).

MATERIALS AND METHODS

Experimental setup

We performed the experiments using the NePTUN 20 TW laser system at Tel Aviv University (*53*). Cartoon schematics of the irradiation setup is shown in Fig. 2A. Thirty-femtosecond-long laser pulses with energies in the range of 100 to 300 mJ (on-target) were focused using an f/2.5 off-axis parabolic mirror unto 800-nm-thick Au or poly(methyl methacrylate) layers, deposited over a freestanding 200-nm-thick SiN membrane (*54*). We measured 70% of the laser energy to be contained within a circle of 5.7-μm diameter. An automated target system delivered the targets to the laser focus at a rate of up to 0.2 Hz (*55*).

The residual energy from the front-end pump laser was used as the source for the engineered pre-pulses. These $\lambda = 532$ nm, $E = 0.03$ to 2 mJ, and $\tau_{pp} = 43$-ps laser pulses are optically synchronized with the main pulse. Before focusing, the pre-pulse was spatially filtered and collimated. A relative delay of $\Delta t_{main}^{pre} = 0$ to 90 ns between the pre- and main pulses was achieved using a multiplane delay line (*56*). Seventy percent of the pre-pulse energy was measured to be contained within a circle of 8.5-μm diameter. Under these different irradiation conditions, we recorded snapshots of their plasma density profiles using the Nomarski interferometric technique (*57*, *58*). The interferometric probe was a second harmonic of the main laser pulse, propagating parallel to the target and perpendicular to the focal axis of the main pulse. We recorded electron spectra using a charge-coupled device imaging a CsI(Tl) scintillator (*59*) at the focal plane of a magnetic spectrometer, described in detail in the supplementary note of (*20*).

PIC simulations

PIC simulations carried out with the EPOCH code (*32*). The simulation space was defined as a (200 μm)$_\perp$–by–(400 to 1200 μm)$_\parallel$ box with (4000)$_\perp$–by–(8000 to 24,000)$_\parallel$ computational mesh cells of size of 50 nm by 50 nm. The laser pulse had a Gaussian temporal profile with a 30-fs width (full width at half maximum), focused to a Gaussian intensity distribution with a waist diameter of 2.62 μm, a wavelength of 800 nm, and in p-polarization. The peak laser intensity was 3.0×10^{19} W cm^{-2} ($a_0 = 3.7$). Simulations ran for a total duration of 1320 to 4600 fs to ensure propagation of the pulse through the full simulation space.

Distinction between DLA and LWFA

The relative contributions of DLA and LWFA to the acceleration of each simulated electron are quantified by considering the integrated work performed on it in the longitudinal and transverse directions (*18*, *38*)

$$W_\parallel = -\int_0^t \frac{2eE_\parallel P_\parallel}{(mc)^2} dt,\ W_\perp = -\int_0^t \frac{2e\vec{E}_\perp \cdot \vec{P}_\perp}{(mc)^2} dt \quad (3)$$

where $E_\parallel P_\parallel$ and $\vec{E}_\perp \cdot \vec{P}_\perp$ are the products of the energy and momentum components in the directions parallel and transverse to the laser direction, respectively. This distinction is a good measure for the dominant acceleration mechanism because, while, for LWFA, the acceleration occurs via the forward-pushing field gradients in the plasma wakes, for DLA, electrons are gaining energy through transverse oscillations, which are later directed forward through $\vec{J} \times \vec{B}$ forces.

REFERENCES AND NOTES

1. W. P. Leemans, A. J. Gonsalves, H. S. Mao, K. Nakamura, C. Benedetti, C. B. Schroeder, Cs. Tóth, J. Daniels, D. E. Mittelberger, S. S. Bulanov, J. L. Vay, C. G. R. Geddes, E. Esarey, Multi-Gev electron beams from capillary-discharge-guided subpetawatt laser pulses in the self-trapping regime, *Phys. Rev. Lett.* **113**, 245002 (2014).
2. A. J. Gonsalves, K. Nakamura, J. Daniels, C. Benedetti, C. Pieronek, T. C. H. De Raadt, S. Steinke, J. H. Bin, S. S. Bulanov, J. Van Tilborg, C. G. R. Geddes, C. B. Schroeder, Cs. Tóth, E. Esarey, K. Swanson, L. Fan-Chiang, G. Bagdasarov, N. Bobrova, V. Gasilov, G. Korn, P. Sasorov, W. P. Leemans, Petawatt laser guiding and electron beam acceleration to 8 GeV in a laser-heated capillary discharge waveguide. *Phys. Rev. Lett.* **122**, 084801 (2019).
3. B. Miao, J. E. Shrock, L. Feder, R. C. Hollinger, J. Morrison, R. Nedbailo, A. Picksley, H. Song, S. Wang, J. J. Rocca, H. M. Milchberg, Multi-GeV electron bunches from an all-optical laser wakefield accelerator. *Phys. Rev. X* **12**, 31038 (2022).
4. J. Faure, C. Rechatin, A. Norlin, A. Lifschitz, Y. Glinec, V. Malka, Controlled injection and acceleration of electrons in plasma wakefields by colliding laser pulses. *Nature* **444**, 737–739 (2006).
5. M. Zeng, M. Chen, L. L. Yu, W. B. Mori, Z. M. Sheng, B. Hidding, D. A. Jaroszynski, J. Zhang, Multichromatic narrow-energy-spread electron bunches from laser-wakefield acceleration with dual-color lasers. *Phys. Rev. Lett.* **114**, 084801 (2015).
6. C. A. Cecchetti, S. Betti, A. Gamucci, A. Giulietti, D. Giulietti, P. Koester, L. Labate, N. Patak, F. Vittori, O. Ciricosta, L. A. Gizzi, High-charge, multi-MeV electron bunches accelerated in moderate laser-plasma interaction regime. *AIP Conf. Proc.* **1209**, 19–22 (2010).

7. E. Brunetti, R. N. Campbell, J. Lovell, D. A. Jaroszynski, High-charge electron beams from a laser-wakefield accelerator driven by a CO_2 laser. *Sci. Rep.* **12**, 6703 (2022).
8. Z. H. He, B. Hou, J. A. Nees, J. H. Easter, J. Faure, K. Krushelnick, A. G. R. Thomas, High repetition-rate wakefield electron source generated by few-millijoule, 30 fs laser pulses on a density downramp. *New J. Phys.* **15**, 053016 (2013).
9. V. Malka, J. Faure, Y. A. Gauduel, E. Lefebvre, A. Rousse, K. T. Phuoc, Principles and applications of compact laser-plasma accelerators. *Nat. Phys.* **4**, 447–453 (2008).
10. S. Fourmaux, E. Hallin, P. G. Arnison, J. C. Kieffer, Optimization of laser-based synchrotron x-ray for plant imaging. *Appl. Phys. B Lasers Opt.* **125**, 34 (2019).
11. A. Pukhov, Z.-M. Sheng, J. Meyer-ter-Vehn, Particle acceleration in relativistic laser channels. *Phys. Plasmas* **6**, 2847–2854 (1999).
12. A. V. Arefiev, A. P. L. Robinson, V. N. Khudik, Novel aspects of direct laser acceleration of relativistic electrons. *J. Plasma Phys.* **81**, 475810404 (2015).
13. S. P. D. Mangles, B. R. Walton, M. Tzoufras, Z. Najmudin, R. J. Clarke, A. E. Dangor, R. G. Evans, S. Fritzler, A. Gopal, C. Hernandez-Gomez, W. B. Mori, W. Rozmus, M. Tatarakis, A. G. R. Thomas, F. S. Tsung, M. S. Wei, K. Krushelnick, Electron acceleration in cavitated channels formed by a petawatt laser in low-density plasma. *Phys. Rev. Lett.* **94**, 245001 (2005).
14. S. Kneip, S. R. Nagel, C. Bellei, N. Bourgeois, A. E. Dangor, A. Gopal, R. Heathcote, S. P. D. Mangles, J. R. Marquès, A. Maksimchuk, P. M. Nilson, K. Ta Phuoc, S. Reed, M. Tzoufras, F. S. Tsung, L. Willingale, W. B. Mori, A. Rousse, K. Krushelnick, Z. Najmudin, Observation of synchrotron radiation from electrons accelerated in a petawatt-laser-generated plasma cavity. *Phys. Rev. Lett.* **100**, 105006 (2008).
15. D. Gorlova, I. Tsymbalov, R. Volkov, A. Savel'ev, Transition radiation in the THz range generated in the relativistic laser–tape target interaction. *Laser Phys. Lett.* **19**, 075401 (2022).
16. G. Malka, E. Lefebvre, J. L. Miquel, Experimental observation of electrons accelerated in vacuum to relativistic energies by a high-intensity laser. *Phys. Rev. Lett.* **78**, 3314–3317 (1997).
17. G. Malka, J. Fuchs, F. Amiranoff, S. D. Baton, R. Gaillard, J. L. Miquel, H. Pépin, C. Rousseaux, G. Bonnaud, M. Busquet, L. Lours, Suprathermal electron generation and channel formation by an ultrarelativistic laser pulse in an underdense preformed plasma. *Phys. Rev. Lett.* **79**, 2053 (1997).
18. C. Gahn, G. D. Tsakiris, A. Pukhov, J. Meyer-Ter-Vehn, G. Pretzler, P. Thirolf, D. Habs, K. J. Witte, Multi-MeV electron beam generation by direct laser acceleration in high-density plasma channels. *Phys. Rev. Lett.* **83**, 4772–4775 (1999).
19. L. Willingale, A. G. R. Thomas, P. M. Nilson, H. Chen, J. Cobble, R. S. Craxton, A. Maksimchuk, P. A. Norreys, T. C. Sangster, R. H. H. Scott, C. Stoeckl, C. Zulick, K. Krushelnick, Surface waves and electron acceleration from high-power, kilojoule-class laser interactions with underdense plasma. *N. J. Phys.* **15**, 025023 (2013).
20. I. Pomerantz, E. McCary, A. R. Meadows, A. Arefiev, A. C. Bernstein, C. Chester, J. Cortez, M. E. Donovan, G. Dyer, E. W. Gaul, D. Hamilton, D. Kuk, A. C. Lestrade, C. Wang, T. Ditmire, B. M. Hegelich, Ultrashort pulsed neutron source. *Phys. Rev. Lett.* **113**, 184801 (2014).
21. O. N. Rosmej, N. E. Andreev, S. Zaehter, N. Zahn, P. Christ, B. Borm, T. Radon, A. Sokolov, L. P. Pugachev, D. Khaghani, F. Horst, N. G. Borisenko, G. Sklizkov, V. G. Pimenov, Interaction of relativistically intense laser pulses with long-scale near critical plasmas for optimization of laser based sources of MeV electrons and gamma-rays. *N. J. Phys.* **21**, 043044 (2019).
22. M. M. Günther, O. N. Rosmej, P. Tavana, M. Gyrdymov, A. Skobliakov, A. Kantsyrev, S. Zähter, N. G. Borisenko, A. Pukhov, N. E. Andreev, Forward-looking insights in laser-generated ultra-intense γ-ray and neutron sources for nuclear application and science. *Nat. Commun.* **13**, 170 (2022).
23. J. Powell, S. Payeur, S. Fourmaux, H. Ibrahim, J. C. Kieffer, S. MacLean, F. Légaré, "100 kev electron beam generation by direct laser acceleration using longitudinal electric fields" in *2021 Conference on Lasers and Electro-Optics (CLEO)* (IEEE, 2021), pp. 1–2.
24. A. Pukhov, Z.-M. Sheng, J. Meyer-ter-Vehn, Particle acceleration in relativistic laser channels. *Phys. Plasmas* **6**, 2847–2854 (1999).
25. O. Rosmej, M. Gyrdymov, M. M. Günther, N. E. Andreev, P. M. Tavana, P. Neumayer, S. J. Zähter, N. Zahn, V. S. Popov, N. Borisenko, A. Kantsyrev, A. Skobliakov, V. Panyushkin, A. Bogdanov, F. Consoli, X. F. Shen, A. Pukhov, High-current laser-driven beams of relativistic electrons for high energy density research. *Plasma Phys. Controlled Fusion* **62**, 115024 (2020).
26. L. Willingale, A. V. Arefiev, G. J. Williams, H. Chen, F. Dollar, A. U. Hazi, A. Maksimchuk, M. J. E. Manuel, E. Marley, W. Nazarov, T. Z. Zhao, C. Zulick, The unexpected role of evolving longitudinal electric fields in generating energetic electrons in relativistically transparent plasmas. *N. J. Phys.* **20**, 093024 (2018).
27. L. Willingale, S. R. Nagel, A. G. R. Thomas, C. Bellei, R. J. Clarke, A. E. Dangor, R. Heathcote, M. C. Kaluza, C. Kamperidis, S. Kneip, K. Krushelnick, N. Lopes, S. P. D. Mangles, W. Nazarov, P. M. Nilson, Z. Najmudin, Characterization of high-intensity laser propagation in the relativistic transparent regime through measurements of energetic proton beams. *Phys. Rev. Lett.* **102**, 125002 (2009).
28. M. Rehwald, S. Assenbaum, C. Bernert, F.-E. Brack, M. Bussmann, T. E. Cowan, C. B. Curry, F. Fiuza, M. Garten, L. Gaus, M. Gauthier, S. Göde, I. Göthel, S. H. Glenzer, L. Huang, A. Huebl, J. B. Kim, T. Kluge, S. Kraft, F. Kroll, J. Metzkes-Ng, T. Miethlinger, M. Loeser, L. Obst-huebl, M. Reimold, H.-P. Schlenvoigt, C. Schoenwaelder, U. Schramm, M. Siebold, F. Treffert, L. Yang, T. Ziegler, K. Zeil, Ultra-short pulse laser acceleration of protons to 80 MeV from cryogenic hydrogen jets tailored to near-critical density. *Nat. Commun.* **14**, 4009 (2023).
29. P. Mora, Thin-foil expansion into a vacuum. *Phys. Rev. E Stat. Nonlin. Soft Matter Phys.* **27**, 056401 (2005).
30. V. L. J. Phung, M. Kim, J. Kim, H. S. Uhm, H. Suk, Characteristics of the preplasma formation using an uncompressed picosecond-long laser pulse with a large spot size on Al and mylar targets. *Curr. Appl. Phys.* **19**, 829–834 (2019).
31. A. Sagisaka, H. Daido, K. Ogura, S. Orimo, Y. Hayashi, M. Nishiuchi, M. Mori, K. Matsukado, A. Fukumi, Z. Li, S. Nakamura, K. Takagaki, H. Hazama, M. Suzuki, T. Utsumi, S. V. Bulanov, T. Esirkepov, Characterization of preformed plasmas with an interferometer for ultra-short high-intensity laser-plasma interactions. *Appl. Phys. B Lasers Opt.* **78**, 919–922 (2004).
32. T. D. Arber, K. Bennett, C. S. Brady, A. Lawrence-Douglas, M. G. Ramsay, N. J. Sircombe, P. Gillies, R. G. Evans, H. Schmitz, A. R. Bell, C. P. Ridgers, Contemporary particle-in-cell approach to laser-plasma modelling. *Plasma Phys. Control. Fusion* **57**, 113001 (2015).
33. M. V. Ammosov, N. B. Delone, V. P. Krainov, "Tunnel ionization of complex atoms and atomic ions in electromagnetic field" in *High Intensity Laser Processes*, vol. 664 (SPIE, 1986), pp. 138–141.
34. V. S. Popov, Tunnel and multiphoton ionization of atoms and ions in a strong laser field (Keldysh theory). *Phys. Usp.* **47**, 855–885 (2004).
35. J. Li, A. V. Arefiev, S. S. Bulanov, D. Kawahito, M. Bailly-Grandvaux, G. M. Petrov, C. McGuffey, F. N. Beg, Ionization injection of highly-charged copper ions for laser driven acceleration from ultra-thin foils. *Sci. Rep.* **9**, 666 (2019).
36. M. A. Purvis, V. N. Shlyaptsev, R. Hollinger, C. Bargsten, A. Pukhov, A. Prieto, Y. Wang, B. M. Luther, L. Yin, S. Wang, J. J. Rocca, Relativistic plasma nanophotonics for ultrahigh energy density physics. *Nat. Photonics* **7**, 796–800 (2013).
37. T. Wang, D. Blackman, K. Chin, A. Arefiev, Effects of simulation dimensionality on laser-driven electron acceleration and photon emission in hollow microchannel targets. *Phys. Rev. E* **104**, 045206 (2021).
38. P. M. King, K. Miller, N. Lemos, J. L. Shaw, B. F. Kraus, M. Thibodeau, B. M. Hegelich, J. Hinojosa, P. Michel, C. Joshi, K. A. Marsh, W. Mori, A. Pak, A. G. R. Thomas, F. Albert, Predominant contribution of direct laser acceleration to high-energy electron spectra in a low-density self-modulated laser wakefield accelerator. *Phys. Rev. Acc. Beams* **24**, 011302 (2021).
39. J. L. Shaw, N. Lemos, L. D. Amorim, N. Vafaei-Najafabadi, K. A. Marsh, F. S. Tsung, W. B. Mori, C. Joshi, Role of direct laser acceleration of electrons in a laser wakefield accelerator with ionization injection. *Phys. Rev. Lett.* **118**, 064801 (2017).
40. R. Wagner, S. Y. Chen, A. Maksimchuk, D. Umstadter, Electron acceleration by a laser wakefield in a relativistically self-guided channel. *Phys. Rev. Lett.* **78**, 3125–3128 (1997).
41. D. Gorlova, I. Tsymbalov, K. Ivanov, A. Zavorotnyi, V. Nedorezov, A. Savel'ev, "Efficient forward direct laser acceleration of electrons in subcritical plasma with injection through hybrid parametric instability" in *Laser Acceleration of Electrons, Protons, and Ions VI; 1177906*, vol. 11779 (SPIE, 2021), p. 4.
42. D. Jung, K. Falk, N. Guler, O. Deppert, M. Devlin, A. Favalli, J. C. Fernandez, D. C. Gautier, M. Geissel, R. Haight, C. E. Hamilton, B. M. Hegelich, R. P. Johnson, F. Merrill, G. Schaumann, K. Schoenberg, M. Schollmeier, T. Shimada, T. Taddeucci, J. L. Tybo, S. a. Wender, C. H. Wilde, G. a. Wurden, M. Roth, Characterization of a novel, short pulse laser-driven neutron source. *Phys. Plasmas* **20**, 056706 (2013).
43. S. S. Dietrich, B. L. Berman, Atlas of photoneutron cross sections obtained with monoenergetic photons. *At. Data Nucl. Data Tables* **38**, 199–338 (1988).
44. S. N. Chen, F. Negoita, K. Spohr, E. D'Humières, I. Pomerantz, J. Fuchs, Extreme brightness laser-based neutron pulses as a pathway for investigating nucleosynthesis in the laboratory. *Matter Radiat. Extremes* **4**, 054402 (2019).
45. M. Zimmer, S. Scheuren, A. Kleinschmidt, N. Mitura, A. Tebartz, G. Schaumann, T. Abel, T. Ebert, M. Hesse, S. Zäahter, S. C. Vogel, O. Merle, R. J. Ahlers, S. D. Pinto, M. Peschke, T. Kröll, V. Bagnoud, C. Rödel, M. Roth, Demonstration of non-destructive and isotope-sensitive material analysis using a short-pulsed laser-driven epi-thermal neutron source. *Nat. Commun.* **13**, 1173 (2022).
46. C. Grünzweig, D. Mannes, A. Kaestner, F. Schmid, P. Vontobel, J. Hovind, S. Hartmann, S. Peetermans, E. Lehmann, Progress in industrial applications using modern neutron imaging techniques. *Phys. Proced.* **43**, 231–242 (2013).
47. T. T. Böhlen, F. Cerutti, M. P. W. Chin, A. Fassò, A. Ferrari, G. Ortega, A. Mairani, P. R. Sala, G. Smirnov, V. Vlachoudis, The FLUKA code: Developments and challenges for high energy and medical applications. *Nucl. Data Sheets* **120**, 211–214 (2014).
48. B., S. Ishkhanov, I. M. Kapitonov, E. V. Lazutin, I. M. Piskarev, V. G. Shevchenko, Photoneutron reactions on copper. *Vestn. Mosk. Univ., Ser. III. Fiz. Astron.* **11**, 606–613 (1970).
49. R. Babjak, L. Willingale, A. Arefiev, M. Vranic, Efficient direct laser acceleration by multi-petawatt lasers. arXiv:2304.10469 [quant-ph] (2023).
50. M. Jirka, M. Vranic, T. Grismayer, L. O. Silva, Scaling laws for direct laser acceleration in a radiation-reaction dominated regime. *New J. Phys.* **22**, 083058 (2020).

51. M. Vranic, R. A. Fonseca, L. O. Silva, Extremely intense laser-based electron acceleration in a plasma channel. *Plasma Phys. Control. Fusion* **60**, 034002 (2018).
52. B. Martinez, B. Barbosa, M. Vranic, Creation and direct laser acceleration of positrons in a single stage. *Phys. Rev. Acc. Beams* **26**, 011301 (2023).
53. E. Porat, A. Levanon, D. Roitman, I. Cohen, R. Louzon, I. Pomerantz, "Towards direct-laser-production of relativistic surface harmonics" in *Relativistic Plasma Waves and Particle Beams as Coherent and Incoherent Radiation Sources III* (SPIE, 2019), p. 17.
54. Y. Gershuni, M. Elkind, I. Cohen, A. Tsabary, D. Sarkar, I. Pomerantz, Automated delivery of microfabricated targets for intense laser irradiation experiments. *J. Vis. Exp.* 10.3791/61056, (2021).
55. Y. Gershuni, D. Roitman, I. Cohen, E. Porat, Y. Danan, M. Elkind, A. Levanon, R. Louzon, D. Reichenberg, A. Tsabary, E. Urisman, S. Vaisman, I. Pomerantz, A gatling-gun target delivery system for high-intensity laser irradiation experiments. *Nucl. Instrum. Methods Phys. Res., Sect. A* **934**, 58–62 (2019).
56. I. Cohen, A. Levanon, D. Roitman, D. Shohat, E. Urisman, I. Pomerantz, "Cat's cradle: A compact, 3D mounted, 90-ns optical delay-line for laser-electron acceleration" in *Laser Acceleration of Electrons, Protons, and Ions V*, vol. 11037, (SPIE, 2019).
57. R. Benattar, C. Popovics, R. Sigel, Polarized light interferometer for laser fusion studies. *Rev. Sci. Instrum.* **50**, 1583–1586 (1979).
58. D. Giulietti, M. Galimberti, A. Giulietti, L. A. Gizzi, R. Numico, P. Tomassini, M. Borghesi, V. Malka, S. Fritzler, M. Pittman, K. Ta Phouc, A. Pukhov, Production of ultracollimated bunches of multi-MeV electrons by 35 fs laser pulses propagating in exploding-foil plasmas. *Phys. Plasmas* **9**, 3655–3658 (2002).
59. A. Pappalardo, L. Cosentino, P. Finocchiaro, An imaging technique for detection and absolute calibration of scintillation light. *Rev. Sci. Instrum.* **81**, 033308 (2010).

Acknowledgments: We acknowledge aid in target fabrication from the Tel Aviv University Center for Nanoscience and Nanotechnology. Simulations were performed using EPOCH, which was developed as part of the UK Engineering and Physical Sciences Research Council (EPSRC) funded project no. EP/G054940/1. **Funding:** I.P. acknowledges the financial support of the Israeli Ministry of Energy, grant no. 220-11-054; the Israel Science Foundation, grant no. 2314/21; and the Zuckerman STEM Leadership Program. A.V.A. acknowledges the support from the National Science Foundation (no. PHY-1903098) and the National Science Foundation - Czech Science Foundation partnership (NSF award PHY-2206777). This work used HPC resources through allocations (i) PHY190034 from the Advanced Cyberinfrastructure Coordination Ecosystem: Services Support (ACCESS) program, which is supported by National Science Foundation grants nos. 2138259, 2138286, 2138307, 2137603, and 2138296; and (ii) TG-PHY190034 from the Extreme Science and Engineering Discovery Environment (XSEDE), which is supported by National Science Foundation grant no. ACI-1548562. I.C. acknowledges support by the Jabotinsky Fellowship of the Ministry of Science and Technology, Israel. **Author contributions:** I.P. and I.C. conceptualized and wrote the manuscript, with feedback from all other authors. I.P. and A.V.A. obtained funding and supervised this project. I.C. performed and analyzed the experiment, with assistance from M.E., A.L., L.P., and Y.G. T.M. performed and analyzed the PIC simulations, with assistance from K.T. **Competing interests:** The authors declare that they have no competing interests. **Data and materials availability:** All data needed to evaluate the conclusions in the paper are present in the paper.

Submitted 8 August 2023
Accepted 12 December 2023
Published 10 January 2024
10.1126/sciadv.adk1947